PERGAMON

International Journal of Heat and Mass Transfer 45 (2002) 343–356

International Journal of HEAT and MASS TRANSFER

www.elsevier.com/locate/ijhmt

Thermocline dynamics in a thermally stratified store

J. van Berkel [1], C.C.M. Rindt *, A.A. van Steenhoven

Department of Mechanical Engineering, Eindhoven University of Technology, WH-3.129, P.O. Box 513, 5600 MB Eindhoven, Netherlands

Received 21 June 2000; received in revised form 6 April 2001

Abstract

Analysis of a stratified store thermocline entrainment process is done by a side-by-side comparison of experiments and a direct numerical simulation. The experimental and numerical analyses are shown to be complementary; where the experiment is a true realisation of the thermocline entrainment process, the numerical simulation provides the temporal and spatial resolution for detailed analysis. The agreement between both is good. It appears that during collision of the buckling jet with the thermocline inhomogeneous penetration and back flow occur. At the point where the jet flows back into the bottom layer, upper-layer fluid is dragged into the bottom layer. After detachment, the dragged-down fluid filament becomes unstable due to overturning motions, resulting in Kelvin–Helmholtz-like waves. Subsequently the fluid filament is completely mixed with bottom-layer fluid by the action of stretching- and-folding stimulated diffusion. From a comparison between 2D- and 3D-simulation results it appeared that for store optimisation 2D-numerical simulations provide sufficient accuracy. © 2001 Published by Elsevier Science Ltd.

Keywords: Entrainment; Jets; Stratified

1. Introduction

This paper concerns erosion of a density interface by a non-buoyant jet. The immediate practical significance lies in the effective storage of hot and cold water in a single tank (stratified storage). The subject, however, is closely related to applications which seek to destroy stratification, e.g. where a jet is applied to remove heavy gases from oil tanks, to erode loose river beds [1], or to destratify chemical reactors, air-ventilated rooms or stratified lakes or reservoirs. More fundamental research has been performed for geophysical purposes, both on full scale (in oceans, lakes and atmosphere) as well as in the laboratory. Comprehensive reviews are given in [2–5].

Knowledge of the thermocline dynamics and the entrainment process in stratified energy stores is limited to empirically derived design guide lines for specific cases [6–8]. In the stratified store application, it has been shown in among others [9] that the store hydrodynamics roughly can be described by a stagnant outlet layer and a turbulent inlet layer. The two zones are separated by the thermocline. In the turbulent layer, the inlet flow is jet-like, see Fig. 1. At the thermocline, entrainment takes place, here defined as the passage of fluid from the upper (stagnant) fluid layer into the lower (turbulent) fluid layer. Flow visualisation inside a laboratory tank has revealed overturning motions near the thermocline zone in front- and side view. The Richardson number is often used to classify entrainment phenomena. Expressed in local quantities the gradient Ri number is defined as

$$Ri_{\mathrm{g}} = \frac{g(\partial\rho/\partial z)}{\rho(\partial u/\partial z)^2}, \tag{1}$$

with g the acceleration due to gravity, ρ the density, z the vertical coordinate and u the velocity in horizontal direction. Following the general classification of Carruthers and Hunt [4], four general mechanisms may be identified for entrainment being engulfment ($Ri_{\mathrm{g}} <$

* Corresponding author. Tel.: +31-40-247-2978; fax: +31-40-243-3445.

E-mail address: c.c.m.rindt@tue.nl (C.C.M. Rindt).

[1] Present address: Entry Technology, Spoorbaanweg 15, 3911 CA Rhenen, Netherlands.

0017-9310/02/$ - see front matter © 2001 Published by Elsevier Science Ltd.
PII: S0017-9310(01)00161-2

Nomenclature

E	entrainment rate
h	thermocline position
Re_i	inlet Reynolds number
Ri_h	global Richardson number
S_{prod}	entropy production
t	time
T	temperature
u_e	entrainment velocity
u_{in}	inlet velocity

Greek symbols

δ	thermocline thickness
λ_{art}	artificial diffusion
λ_b	buckling wavelength
λ_c	contact length
λ_{k-h}	Kelvin–Helmholtz wavelength
λ_{phys}	physical diffusion
λ_s	length scale spanwise vortices
λ_w	jet width
ξ	measure for artificial diffusion

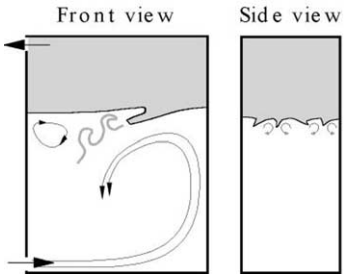

Fig. 1. Schematic representation of the two-layer stratified flow field.

$O(10^{-1})$), overturning ($Ri_g \cong O(10^{-1})$), cusps ($Ri_g \cong O(10^0)$) and wave breaking ($Ri_g > O(10^0)$).

The goal of the present research is to shed light on the thermocline dynamics and the accompanying entrainment mechanisms. Besides, the usefulness of 2D calculations for store optimisation purposes will be discussed briefly. First, the store abstraction is discussed, in conjunction with the numerical and experimental techniques applied. Then the thermocline dynamics is described in great detail focussing on the jet hydrodynamics and entrainment characteristics. Finally, a comparison is made between 3D- and 2D-simulation results and some conclusions are drawn.

2. Store abstraction and process parameter definitions

For short-term (hours) stores the efficiency is dominated by mixing and diffusion processes over the interface separating the high- and low-temperature fluid layers. To avoid destratification much attention has been paid to the design of the inlet diffusers. Vertical cylindrical tanks are frequently equipped with radial disk diffusers, whereas horizontal cylindrical and box-like tanks are usually equipped with linear diffusers. However, in all these systems destratification still takes place via jet-like flows which collide with the thermocline, enhancing mixing and diffusion. As detailed observation of the thermocline entrainment processes in a stratified store tank is hindered by the vertical motion of the thermocline, detailed experiments are done in a specially designed tank. The tank, and the numerical representation, consists of an adiabatic box, enclosing two water layers of different temperatures, see Fig. 2. Water is injected through a slot in the bottom plate and is withdrawn exactly at the same flow rate through the permeable bottom plate. As a result of the zero net inflow, the thermocline advances due to entrainment only, see [10].

The entrainment rate, defined as the upward velocity of the thermocline u_e, divided by the jet inlet velocity u_{in}, can be derived to be [11]

$$E = \frac{u_e}{u_{in}} = C\frac{A_{in}}{A_{plan}}Ri_h^{-1}, \tag{2}$$

where A_{in} is the inlet area, A_{plan} the tank plan area and Ri_h the 'global' Richardson number defined as

$$Ri_h = \frac{g\beta\Delta Th}{u_{in}^2}, \tag{3}$$

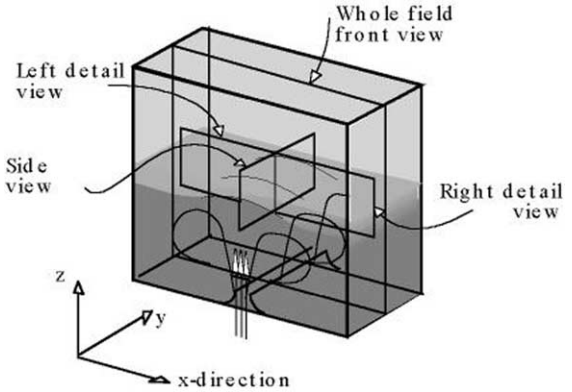

Fig. 2. Jet destratifying box model.

with β the coefficient of thermal expansion, ΔT the temperature difference between the top and bottom layer and h the relative position of the thermocline with respect to the bottom plate. The constant C in Eq. (2) equals 1.0 when the outflow is adiabatically and aerogonically recirculated to the inflow (no net buoyancy flux). When, however, the inlet has a constant temperature (equal to the initial bottom layer temperature) a net buoyancy flux over the bottom boundary of the tank is present. In that case it can be derived that the constant equals 0.5. Irrespective of the constant, it appears that the entrainment rate is a -1 power law which fits the general expression found in [12].

In addition to the entrainment velocity as a measure for the mixing rate, the entropy production rate has been used. In a fluid dynamic system, entropy is produced by diffusion of impulse and diffusion of thermal energy, see for example [13]. The entropy production rate per unit volume reads

$$\dot{s}_{\text{prod}} = \left[\frac{2\eta \boldsymbol{D} : \boldsymbol{D}}{T} + \lambda \left(\frac{|\nabla T|}{T} \right)^2 \right]^2. \tag{4}$$

The first term is the production of entropy due to diffusion of kinetic energy. It represents the amount of viscous work (expressed by the deformation rate tensor $\boldsymbol{D}$ and the dynamic viscosity η) which is dissipated at a temperature T. It can be shown, see [14], that, under practical conditions, this term is negligible compared to the second term, which represents the entropy production rate due to diffusion of heat, with λ the coefficient of conduction.

In general the Ri_h number and the inlet Reynolds number Re_i will be used to characterise the situation under consideration, with the inlet Reynolds number defined as

$$Re_i = \frac{u_{in} w \rho}{\eta}, \tag{5}$$

with w the width of the injection slot. It is worthwhile to mention that Ri_h in the present study is set via the inlet velocity u_{in}. This means that there is a direct coupling between Ri_h and Re_i. Results will be presented for the base case $Ri_h = 20$, $Re_i = 475$, which is a mild case with respect to storage mixing. Results for two and four times higher inlet velocities (corresponding with $Ri_h = 5$, $Re_i = 950$, and $Ri_h = 1.25$, $Re_i = 1900$) are not found to differ qualitatively. Both experimentally and numerically, however, the higher forcing rates are harder to analyse.

3. Numerical model

3.1. General code description

2D and 3D simulations have been performed for the stratified box. With regard to the simulations, common assumptions are made for the physics i.e. Boussinesq approximation, no viscous dissipation of mechanical energy, no radiative heat transfer. The equations to be solved then read

$$\nabla \cdot \mathbf{u} = 0, \tag{6}$$

$$\frac{\partial \mathbf{u}}{\partial t} + \nabla(\mathbf{u} \cdot \mathbf{u}) = -\frac{1}{\rho} \nabla p + \mathbf{g}\beta(T - T_{av}) + \nu \nabla^2 \mathbf{u}, \tag{7}$$

$$\frac{\partial T}{\partial t} + \nabla \cdot (\mathbf{u} T) = \alpha \nabla^2 T. \tag{8}$$

Here p is the reduced pressure, $\mathbf{u}$ the velocity vector, T the temperature, $\mathbf{g}$ the vector representing the acceleration due to gravity, T_{av} the average temperature in the domain, ν the kinematic viscosity and α the thermal diffusivity. Due to the relatively low Reynolds values, no turbulence model was incorporated in the numerical program. The thermocline entrainment process is simulated using a finite difference/volume method with an equidistant orthogonal mesh for the discretisation of equations (with staggered pressure and velocity points). For a large part the code is similar to the marker-and-cell (MAC) formulation presented in [15]. The present code is an adapted version of the code originally employed by Nieuwstadt [16] and modified by Bastiaans et al. [17].

In essence the method is a pressure-correction method. It projects an intermediate velocity field $\mathbf{u}^*$ obtained from the Navier–Stokes equation (excluding pressure), to a divergence-free velocity field $\mathbf{u}^{n+1}$ by evaluating the pressure gradient term in the separate correction/projection step. In this step, a resulting Poisson equation for pressure is solved directly using a finite difference approximation. Discretised in time the equations read

$$\frac{\mathbf{u}^* - \mathbf{u}^{n-1}}{2\Delta t} = -\nabla \cdot (\mathbf{u} \cdot \mathbf{u})^n + g\beta(T - T_{av})^n + \nu \nabla^2 \mathbf{u}^{n-1}, \tag{9}$$

$$\frac{\mathbf{u}^{n+1} - \mathbf{u}^*}{2\Delta t} = -\nabla p^{n+1}, \tag{10}$$

with

$$\nabla \cdot (-\nabla p^{n+1}) = -\nabla^2 p^{n+1} = \nabla \cdot \left(\frac{\mathbf{u}^{n+1} - \mathbf{u}^*}{2\Delta t} \right) = -\nabla \cdot \left(\frac{\mathbf{u}^*}{2\Delta t} \right). \tag{11}$$

For the energy equation,

$$\frac{T^{n+1} - T^n}{\Delta t} = -\nabla \cdot (\mathbf{u} T)^n + \alpha \nabla^2 T^n. \tag{12}$$

For the advection and buoyancy components of the momentum equation, time stepping is performed according to the time central, second-order accurate, neutrally stable leap-frog scheme. As a time central treatment is unconditionally unstable for diffusion, this

term is treated with an Euler forward scheme over $2\Delta t$. To attain second-order accuracy for the treatment of buoyancy, this term is evaluated at time level midpoint n. Splitting between odd and even time levels is avoided by means of a time filter. To ensure stability the time step is limited by the criterion derived in [18], which is based on advective and diffusive constraints.

Care was taken to assure an accurate discretisation of advection (of momentum and thermal energy), as it is associated with the concept of artificial diffusion (of momentum and thermal energy), see [19]. When larger than physical diffusion, artificial diffusion may make numerical simulations highly inaccurate, especially with respect to evaluation of the entropy production rate. To improve accuracy, the advection terms in the impulse equation and in the temperature equation are discretised in a conservative form, see [14].

3.2. Boundary and initial conditions

Boundary conditions are implemented using a shell of virtual cells which enclose the flow domain. Four types of boundaries are used: inlets, outlets, closed walls and periodic walls. For pressure, the homogeneous Neumann condition is used everywhere. For open boundaries (inlet and outlet) this condition implicitly implies a 1D, shear-free, stationary, non-buoyant flow. The physically incorrectness of this boundary condition is assumed to have only a marginal effect as the conditions are restricted to the small inlets (and outlets). For the velocity component normal to the boundary the Dirichlet condition is applied (with non-zero values for the inlet and outlet). The tangential component is set zero everywhere. The temperature boundary conditions are set adiabatic (homogeneous Neumann) for the walls. While the inlet temperature is prescribed in a Dirichlet sense, the outlet temperature is prescribed on the basis of the discretised 1D advection equation, which, unlike the homogeneous Neumann temperature condition, facilitates passage of a temperature gradient zone. For the periodic front and back walls, the virtual cell values for velocity, temperature and pressure are taken equal to the values of the inner cells at the opposite wall (periodic boundary conditions).

All simulations are started with a zero-velocity field. To attain steady-state conditions faster, the initial temperature distribution is prescribed according to an error function profile, representing a two-layer stratification with a diffusive interface. The inlet velocity in the jet simulations increases sinusoidally from zero to the end value in 10 s and is kept constant after this transient. More information on the discretisation of advection and the implementation of the boundary conditions can be found in [10].

The 3D simulation is performed on a $178 \times 160 \times 40$ grid (comprising over 1.1×10^6 cells), which is a compromise between accuracy and CPU time. The question of whether or not this resolution is sufficient to produce a converged solution is discussed later, together with the applicability of 2D-numerical simulations for store optimisation.

4. Experiments

4.1. The experimental set-up

Fig. 3 shows the test set-up used. The domain of interest is sized width $\times$ depth $\times$ height $= 445 \times 245 \times 400$ mm. The size is chosen so as to obtain easy observation of the transport processes and to achieve representative Reynolds and Richardson numbers. At the same time the tank size is kept small to facilitate easy manufacturing and operation.

Injection takes place through a centrally placed, 15 mm wide slot rounded at its outlet. The jet is located in the (ambient temperature) bottom layer so as to suppress circulation system heat losses, which would have occurred had the jet been placed in the hot top layer. Withdrawal takes place through 8×12 uniformly distributed, 1 mm diameter holes on either side of the slot. Flow stabilisation chambers ensure uniform withdrawal and injection. As it is experimentally very difficult to inject fluid with the desired flow rate at a precise constant temperature (as is done in the simulations), fluid is simply withdrawn from the box and returned to the box via hoses, a centrifugal pump with flow adjustment valve and a flow rate meter. To reduce the effect of dissipated pump power on the inlet buoyancy flux the pump is controlled by a variable power supply instead of controlling the mass flow by a flow resistor.

Two-layer stratification is attained by means of an immersed electrical heater, which heats up the top layer to a temperature of 40–45°C. After careful removal of the heater, the top layer is carefully stirred to obtain a uniform top-layer temperature. At the start of the test,

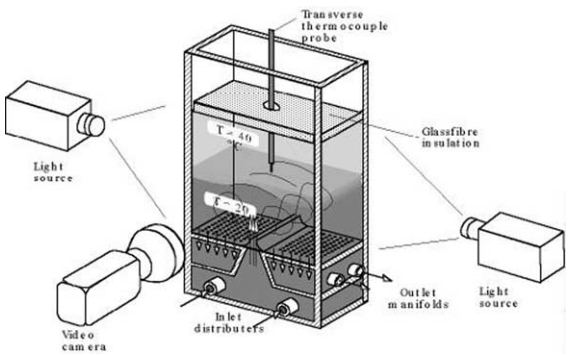

Fig. 3. Stratified box test set-up.

the bottom layer has a temperature equal to the ambient temperature of 20°C. During the tests, an insulation plate, floating on top of the free surface, prevents excessive heat loss and free surface effects.

4.2. Experimental techniques applied

Flow visualisation is done by means of fluorescent dye colouring. In this case a 10–15 mm thick vertical light sheet is created by illuminating the domain from both sides through slotted masks, attached to the side walls, thereby creating a two-dimensional cut of the flow field. The domain content is prepared by adding premixed fluorescent dye in a mass ratio of 1:2000. The dye is added to the hot water only; the colour pattern then visualises the entrainment process in the bottom layer.

Quantitative flow field information is obtained by particle tracking velocimetry (PTV), using the DigImage package version 2.0, see [20]. In application of this technique, the fluid flow velocity is derived by dividing the spatial shift of particles (which have been added to the fluid) by the time between the two recordings. Throughout the experiments, polymer OptImage particles with a nominal diameter of 250 μm are used, in a mass concentration of 1:200 000 for the whole field view or 1:100 000 for the detail view (see Fig. 2). The PTV technique is applied in a standard setting, and is therefore not discussed further.

Application of the PTV routine yields 8 bit deep velocity values on unstructured locations (the position of the identified particles), with a window size of 512×512 pixels and with a time spacing of 0.04 s (25 Hz). To achieve a higher accuracy, the velocity fields have been derived from five subsequent frames, incorporating the condition that a specific particle is recognised in all five subsequent frames, see [20]. In addition, anomalous vectors caused by improper matching are removed by an additional filter. This filter eliminates velocity vectors with a magnitude larger or smaller than the sum of the average magnitude and two times the standard deviation in a certain search area around that vector. Finally, for ease of comparison with the simulations and for ease of computing spatial derivatives and statistics, the unstructured velocity field is spline-interpolated on an equidistant, rectangular grid.

The accuracy of the velocity ranges between 2 and 1 mm s^{-1} for the whole and detailed field windows (see Fig. 2), respectively, which corresponds with the 0.1 subpixel accuracy specified in [20]. Here it should be mentioned that the accuracy of spatially derivative quantities like vorticity is considerably lower. In the PTV routine, typically 500 particles are matched. If the particles are imagined to be distributed uniformly over the 0.12 m^2 (whole field) and 0.03 m^2 (detailed field) windows, the average distance between particles is about 8 and 4 mm, respectively. As a result, it can be derived that the spatial detection limit for vorticity (given an order of magnitude for the velocity of 10 mm s^{-1} and a shear-layer thickness of 10 mm) amounts to 0.25 and 0.12 s^{-1}, respectively. These values are only one order of magnitude smaller than the expected maximum value of the vorticity. Consequently, the PTV results should be interpreted with care.

The centreline temperature profile is recorded using a vertical, linearly traversing probe consisting of a ceramic tube with a co-axially protruding ϕ 0.5 K-type thermocouple, having a response time (in water) of less than 0.1 s. Tests showed typical values for the random error of 0.05°C. Temperature data were recorded at a sample rate of 10 Hz.

5. Thermocline dynamics

As already mentioned, results will be presented for the base case $Ri_h = 20$, $Re_i = 475$. Most of the experimental and numerical results are shown at a time level where the flow has developed to a quasi-steady state. The most apparent flow phenomena observed during the experiment are illustrated in Fig. 4.

5.1. Jet buckling, penetration and rebound

Immediately after flow initiation, a symmetric, mushroom-shaped dipole is formed, which travels towards the thermocline. Upon collision with the thermocline, overshoot and rebounding of the dipole occurs, similar to the vortex/interface collision process described in [21]. After a few rebounds, the thermocline perturbation stabilises and a quasi-steady state develops in which the thermocline temperature and velocity profiles only change shape on a time scale much longer than the convective time scale h/u_{in}, which for the base case is equal to O(10) s. During the quasi-steady state, the general flow pattern is best represented by a snapshot of the fluorescent dye experiments and the calculated temperature distribution, respectively, see Fig. 5.

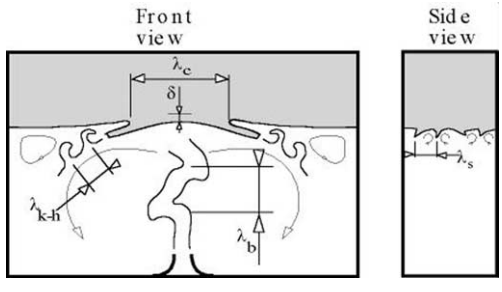

Fig. 4. Schematic drawing of front- and side-view flow phenomena.

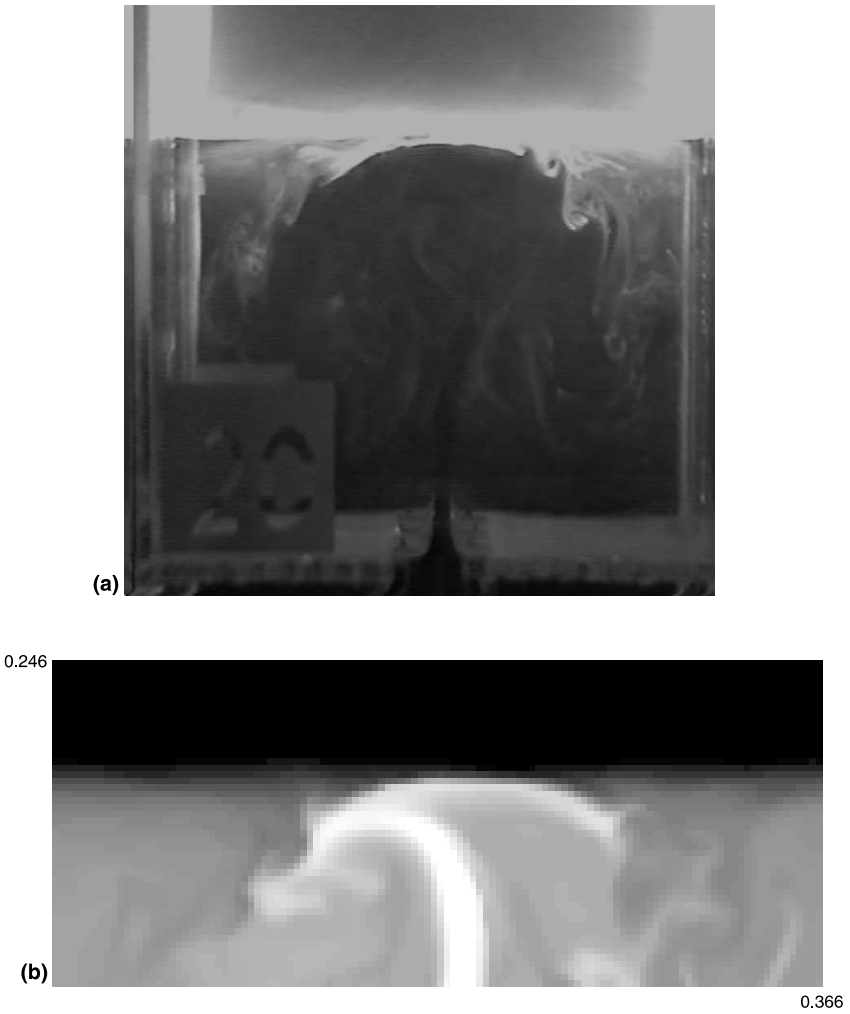

Fig. 5. (a) Whole field (front view) fluorescent dye image. (b) Calculated temperature distribution (white = 20°C, black = 40°C).

The meandering shape of the jet was clearly visible in both the experiments and the calculations. Time and length scale recordings during the experiments indicate a swaying frequency of 0.2–0.3 Hz, a jet width of $\lambda_w = 35 \pm 5$ mm and a buckling wavelength of $\lambda_b = 60 \pm 10$ mm (see Fig. 4). These values correspond with the estimates presented in [22], on the basis of bending stiffness of a flow tube and its longitudinal compressive (pressure) forces, where it was found that $\lambda_b = 1.81\lambda_w$.

Not visible in Fig. 5 is the shear-layer instability near the jet inlet, between the jet and the surrounding fluid. As reported in [23], even for low-Reynolds-number jets the shear layer originating from the nozzle lip is inviscidly unstable via the Kelvin–Helmholtz instability mechanism. Though observed by eye, this instability is not captured by the PTV and numerical simulation techniques, probably due to insufficient spatial resolution.

As already mentioned, when jet fluid enters the upper layer, its upward momentum is annihilated as a result of negative buoyancy. Kinetic energy is temporarily converted into potential energy and released when the jet fluid falls back into the bottom layer. As a result of regained downward momentum, the jet fluid does not spread laterally along the thermocline, but penetrates into the bottom layer. As a consequence of the rebound process, the contact area between the jet and the upper layer has a finite span width λ_c, see Fig. 4. On the basis of video tape recordings of the experiments, a span width of $\lambda_c = 100$ mm is estimated, which is approximately 1/4 of the tank width.

5.2. Shear-layer instability

A remarkable feature is that the collision area between the jet and the stagnant upper-layer fluid is

smooth and stable, whereas a shear-layer instability develops on both sides of the collision area (see Fig. 5). It is here postulated that, in the collision region, the necessary condition for shear-layer instability, $Ri_g < 0.25$, see [13], is not satisfied. Temperature profile measurements showed that the temperature gradient has an order of magnitude of 1000°C m^{-1}. The centreline velocity gradient, which can be derived from the momentary velocity fields, has a value of 0.75 s^{-1}, which is quite moderate as the flow in the collision area is stagnating. Using these figures, the centreline gradient Richardson number, Eq. (1), can be calculated to be about $Ri_g = 5$, which is well above the critical value of 0.25. Near the edges of the collision area, however, the temperature gradient becomes less due to diffusion, while at the same time, the velocity gradient increases because the fluid moves away from the stagnation area. Due to these effects, the Ri_g number decreases and a shear-layer instability develops. In addition, it may be argued that shear-layer roll-up needs time to develop. An analysis of an unstable shear layer has been performed in [22]. Estimates are derived for the diameter of the first roll and for the stable length before the first roll occurs (in the present study denoted as $1/2\ \lambda_c$). Given an average velocity of 10 mm s^{-1}, an estimate for the diameter of the first roll of 6 mm is calculated, which roughly agrees with the observations in the present study. Furthermore, a stable length of about 20 mm is calculated, which is about half the value found in the present study.

The Kelvin–Helmholtz shear-layer instabilities found in the present investigation (see Fig. 5) are in accordance with the 'lateral vortices' found in [24] using a similar experimental set-up. However, where Cotel suggests that the vortices cause entrainment, the present study indicates that they are formed after shear-layer detachment,

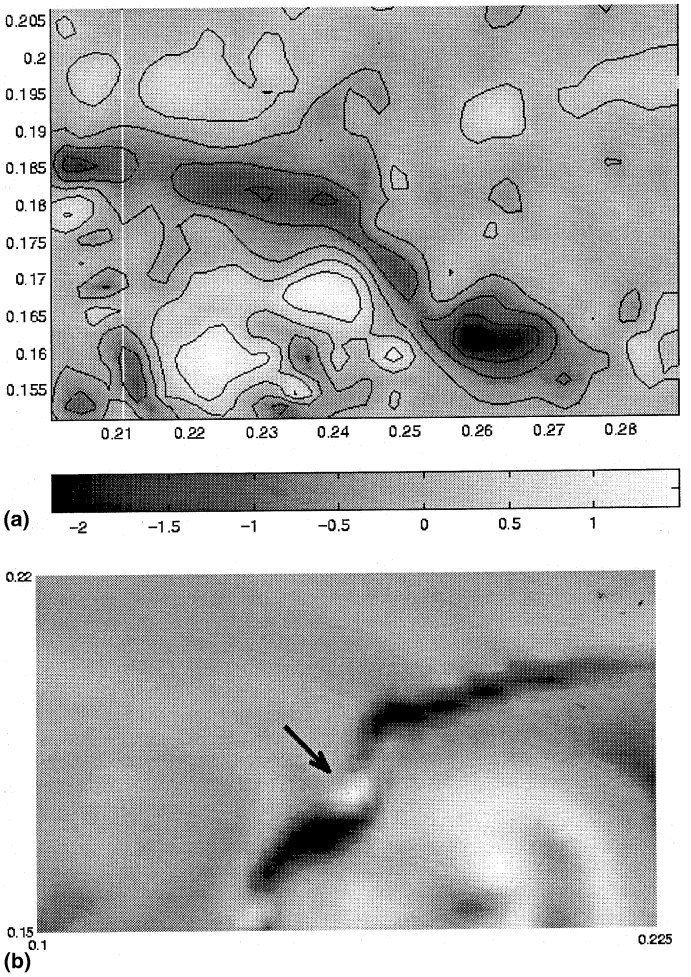

Fig. 6. (a) Right detail view of measured shear layer vorticity. (b) Left detail view of calculated shear layer vorticity (black = +2 s^{-1}, white = −2 s^{-1}).

when top-layer entrainment has already taken place. The mechanism for the generation of the vortices is most likely the Kelvin–Helmholtz instability mechanism, caused by accumulation of vorticity in the shear layer between the deflected jet and the surrounding fluid. It is found that the wavelength of the Kelvin–Helmholtz waves λ_{k-h} (see Fig. 4) increases with the distance from the collision area. Upon birth the wavelength is approximately $\lambda_{k-h} = 30$ mm. A shedding frequency is estimated which is close to the 0.2–0.3 Hz jet swaying frequency found previously. This may indicate that the shear layer instability is connected to (perhaps triggered by) the buckling motion of the jet.

Based on the Ri_g number it can be concluded that in the collision area the entrainment mechanism ranges between cusps ($Ri_g \cong O(10^0)$) and wave breaking ($Ri_g > O(10^0)$), see [4]. At the position where overturning motions take place ($Ri_g \cong O(10^{-1})$) the shear layer has already detached from the upper layer and entrainment is not expected to play an important role there.

In Fig. 6 the experimentally and numerically derived results for the shear layer vorticity are shown. It supports the general agreement between the experiments and the numerical simulations; though the window sizes and positions are not identical, the overall appearance of the vorticity plots look similar. The x-coordinates of the main vorticity nodes for the experiment ($x = 0.23$ m and $x = 0.26$ m) also indicate a 30 mm distance between two subsequent waves. In addition, though vaguely, production of negative vorticity can be noticed in the tail of the main Kelvin–Helmholtz node, marked by the arrow. As the vorticity is confined to a region in or close to the overturning Kelvin–Helmholtz wave, it is most probably caused by baroclinic effects. This phenomenon, however, is not observed in the experiments, possibly due to a too coarse particle distribution.

5.3. Spanwise instability

Vortices just below the thermocline are also found in the side-view images, see Fig. 7. It is suggested that these spanwise vortices are a result of inhomogeneous jet penetration into the top layer. Due to the relatively high level of negative buoyancy at the stations with large overshoot, return flow occurs to places with a weaker

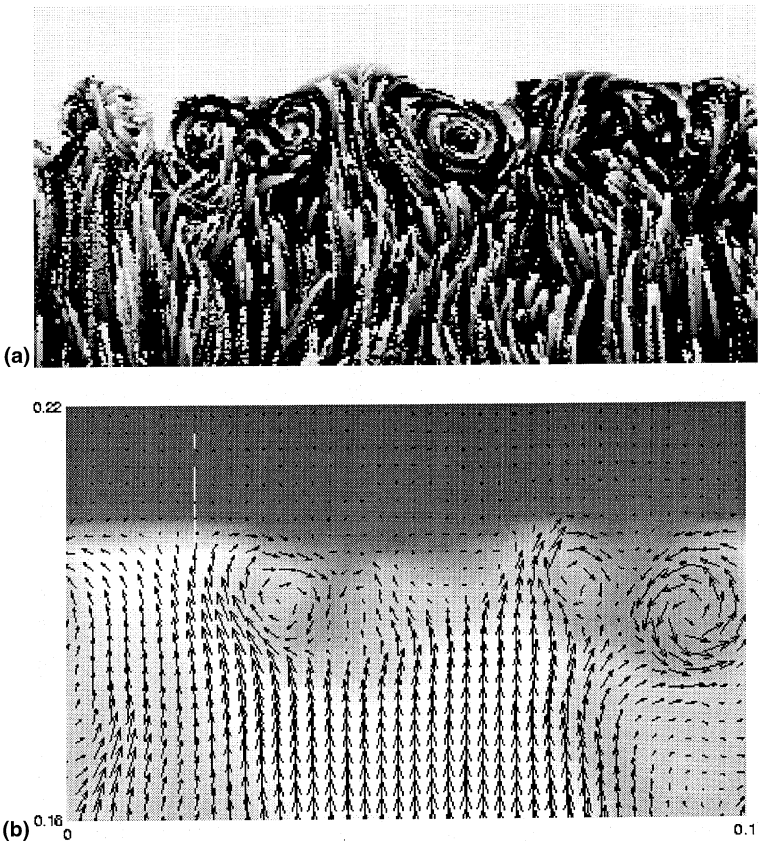

Fig. 7. (a) Side view (200 mm wide) of combined fluorescent dye/particle streak experiment (the white top part is the stagnant layer). (b) Side view (100 mm wide) of calculated velocity vectors and temperature distribution (white = 20°C, black = 40°C).

vertical jet momentum. At spanwise stations where the return flow collides, the flow is deflected further downwards, resulting in the spanwise vortices, see Fig. 7. The cause for inhomogeneous jet deflection and overshoot is looked for in the upstream direction. In Fig. 8 velocity vectors and a contour map of temperature are shown in four horizontal slices, which cut the vertical jet at the $z = 100$, 150, 175 and 200 mm level (measured from the bottom of the tank). The isotherms show that the jet is not homogeneous over the depth, but starts to twist right from its origin. The distortion develops further downstream (upward direction) and seems to evolve in inhomogeneous overshoot. In Fig. 8 this becomes apparent by the lobe-and-cleft structure, similar to that presented in [25] for density currents, where relatively light fluid is overrun by the more dense gravity current. Whether or not the observed jet distortion is a result of intrinsic instability of the jet itself, see [26], or a result of external sources (impingement of vortices present in the bottom layer) needs further investigation.

The spanwise vortices have strong similarities with the spanwise Görtler vortices found in [27] near the density interface in a stratified lid-driven cavity. For the present case, the Görtler instability explanation is unlikely as the vortices are observed also in the jet collision area (in which the flow stagnates) and are not found in the typical Görtler arrangement of adjacent rows.

Quantitative information about the overshoot dynamics is provided by the temperature signal which is monitored at a fixed position along the vertical symmetry axis in the overshoot region, see Fig. 9. Shown are 50 s long time intervals, taken when the local time-averaged temperature is equal to the average of the upper- and bottom-layer temperature (note that for the experiment the temperatures are slightly higher).

The low spectral power present for frequencies higher than 0.5 Hz indicates that the physical time scale is larger than 2 s. Though the power spectrum of the experimental temperature signal appears to be somewhat lower than its numerical equivalent, both spectra yield a remarkable peak for a frequency of 0.18 Hz (denoted by the vertical dashed line). The finding that the peak frequency lies close to the jet buckling frequency of 0.2–0.3 Hz suggests that, like the Kelvin–Helmholtz waves discussed earlier, the thermocline oscillation is connected with the jet swaying motion.

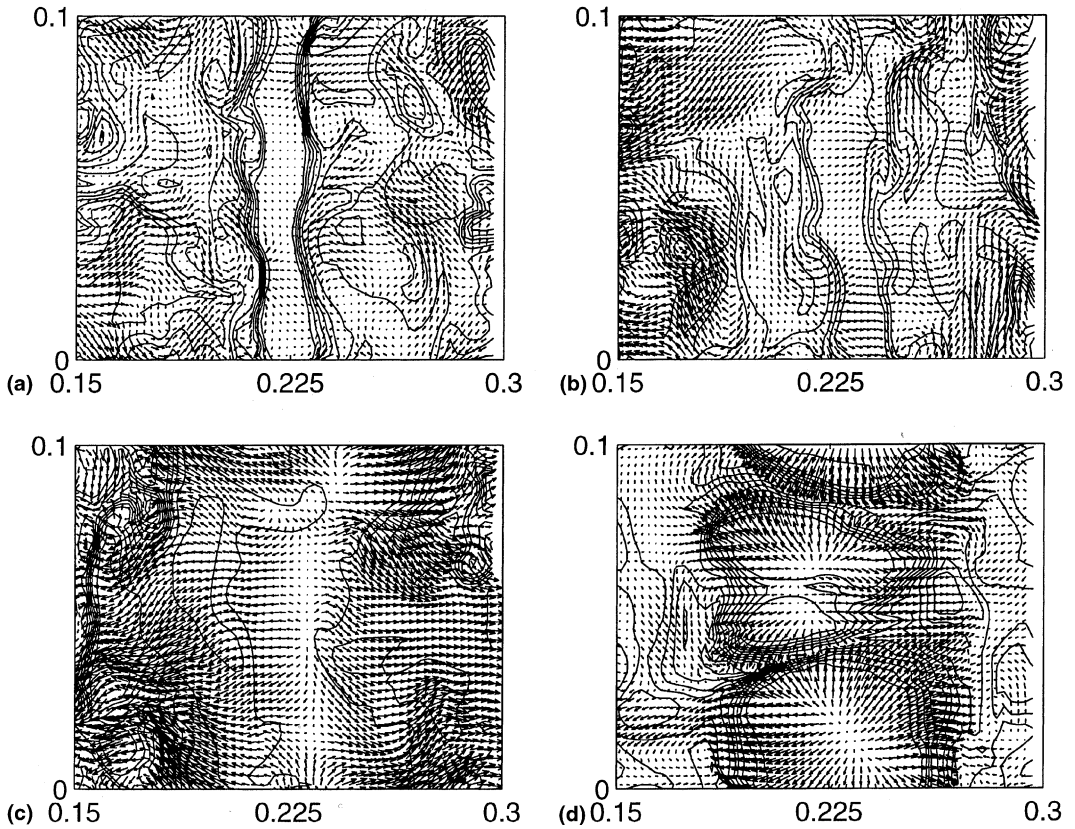

Fig. 8. Calculated top view of velocity vectors and temperature contours in horizontal planes at (a) $z = 100$, (b) $z = 150$, (c) $z = 175$ and (d) $z = 200$ mm. At the jet centreline the thermocline is positioned at about $z = 200$ mm (see also Fig. 7).

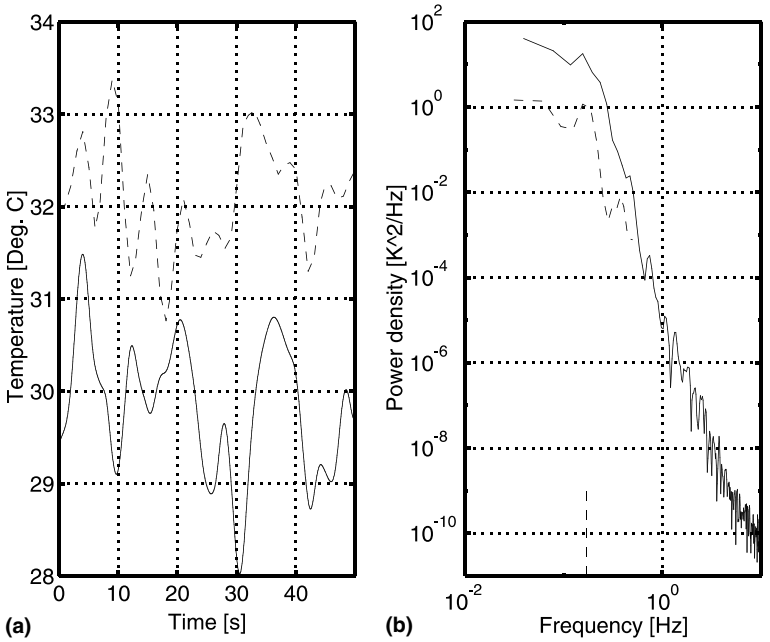

Fig. 9. (a) Temperature signal during thermocline passage. (b) Corresponding spectra. Solid lines: simulation, dashed lines: experiment. The numerical and experimental sample rates are 20 and 1 Hz, respectively.

On the basis of video tape recordings, it is observed that occasionally the vortices present (which have a typical size of $\lambda_s = O(10)$ mm, see Fig. 4) entrain small amounts of top-layer fluid in a way quite similar to the cusps mechanism for $Ri_g \cong O(10^0)$ as found in [4].

5.4. Bottom-layer mixing

Downstream from the collision area, interaction between the deflected jet flow, the spanwise vortices and the Kelvin–Helmholtz waves results in a time-dependent 3D flow pattern which (with the present experimental equipment) cannot be traced any more. An impression can be obtained though from the 3D-numerical simulation results, in which the flow pattern is visualised by means of the entropy production rate per unit volume.

From Fig. 10, it can be concluded that entropy is mainly produced within the thermocline (where heat diffuses from a relatively high temperature to a lower temperature). In the upper layer, where temperature gradients are absent, no entropy is produced. In the bottom layer, however, filaments are visible which are mixed and still diffuse thermal energy. It appears that mixing inside the store is a two-stage process. First, fluid is withdrawn from the thermocline by shear forces exerted by the rebounding jet fluid. Once drawn into the bottom layer, stretching and folding takes place. Due to the increased interface area and decreased normal width, diffusion of heat becomes active. It furthermore becomes clear that this diffusion process is so effective that entrained filaments, once drawn into the bottom layer, do not survive and hence cannot transport thermal energy back to the thermocline.

5.5. Entrainment rate

The entrainment velocity is determined experimentally by the time span necessary for the thermocline to cross two different positions of the thermocouple probe. For the simulation it can be (in steady state) determined from the thermal energy outflux. In Table 1 the values for the entrainment rate at $Ri_h = 20$ are given for both the experiment and the 3D calculation together with the used grid and time step.

It is found that the 3D-numerical result for $Ri_h = 20$ is approximately 70% larger than the experimental result. During the experiments the inlet temperature may differ from the withdrawal temperature by dissipation of pump power and heat losses in the water circulation hoses. With respect to this point, it must be noted that heat losses have an adverse effect on the entrainment rate. However, as the present experimental results compare reasonably well with the findings of others, the discrepancy is probably attributable to inaccuracies in the numerical simulation. A hypothetical explanation for the higher numerically predicted entrainment rate is the presence of artificial diffusion in the numerical simulation. It will be shown that, in case of 2D, the en-

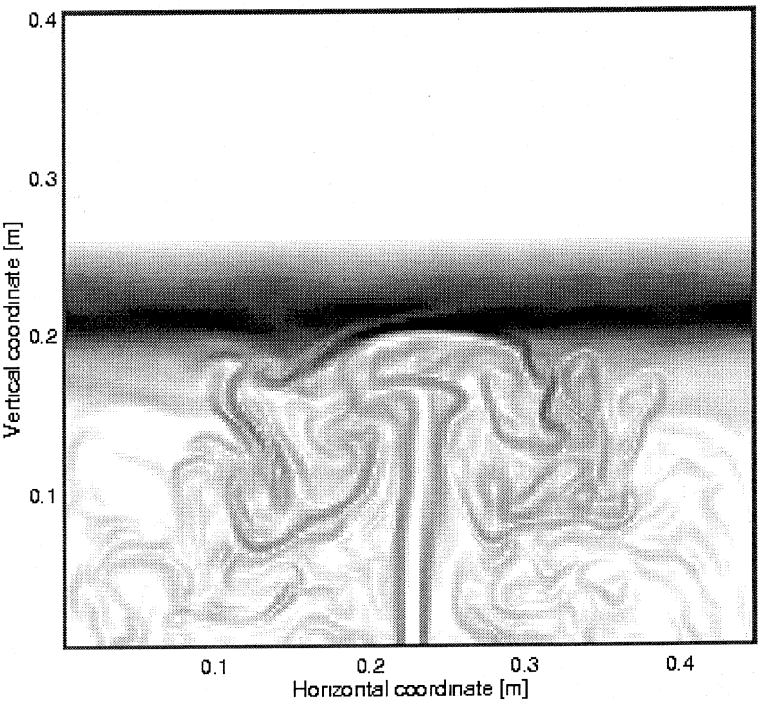

Fig. 10. Calculated entropy production rate in the front-view symmetry plane (white = 10^{-5} W m^{-3} K^{-1}, black = 10^{1} W m^{-3} K^{-1}).

Table 1
Entrainment rate for 3D calculation and experiment for $Ri_h = 20$

Grid, Δt (s)	$ERi_h \times 10^{-3}$ (–)
$178 \times 160 \times 40$, 0.05	9.43
Experiment	5.60

trainment rate and the level of artificial diffusion decreases for finer grids. Hence, it may be expected that, particularly for the 3D simulation, which due to the smaller fluid motion length scales is more susceptible for artificial diffusion effects, the entrainment rate is overpredicted.

6. Comparison with a 2D simulation

In the previous section, it has been shown that the numerical model is at least able to represent the thermocline dynamics found in the experiments in a qualitative sense. Jet buckling phenomena, and shear-layer and spanwise instabilities are predicted in a correct way. Also in a quantitative sense the agreement is rather good. For example the frequencies of the instabilities and the dimensions of the lateral and spanwise vortices are of the same order. The largest difference is found in the entrainment rate which may be due to artificial diffusion. Because grid refinement was not possible for the 3D case due to the limited computer power available, the influence of refinement on the entrainment rate and artificial diffusion is studied for the 2D case.

For an advancing steady thermocline, the entropy production may be calculated on the basis of the momentary temperature field (Eq. (4)), but also from the difference between the gain of entropy of the entrained layer and the entropy which during entrainment has flowed out of the system. The latter is directly connected with the net thermal energy flux which flows out of the system. When a numerical simulation is free of artificial diffusion, both calculation principles yield the same result, see [14]. However, when artificial diffusion is present, the difference between the two values is a measure for the level of artificial diffusion:

$$\xi = \frac{\lambda_{\text{phys}} \int (\nabla T/T)^2 \, \mathrm{d}V}{1/2 u_e \rho c_p (\Delta T/T)^2}.$$

The deviation of ξ from unity is a measure of the rate of artificial diffusion, according to

$$\frac{\lambda_{\text{art}}}{\lambda_{\text{phys}}} = \frac{1-\xi}{\xi}.$$

In Table 2 the values for the entrainment rate are shown for a number of 2D simulations performed for the same conditions, together with the kinetic energy and the

Table 2
2D convergence tests

Grid, Δt (s)	$ERi_h \times 10^{-3}$ (–)	$e_{kin} \times 10^{-6}$ (J kg^{-1})	ξ	CPU time
89 × 80, 0.08	13.4	18.0	0.35	1/2 h
178 × 160, 0.04	13.2	31.1	0.50	3 h
356 × 320, 0.02	11.8	28.0	0.69	1 day
712 × 640, 0.01	10.3	30.3	0.89	1 week

coefficient for artificial diffusion. Also the used computation times are mentioned for a time span of 300 s.

A first thing to notice is that, for the 2D simulations, the kinetic energy level seems to stabilise with grid refinement (some variance persists as the momentary kinetic energy level fluctuates). This indicates that a more or less converged solution is obtained for the momentum equation. Furthermore it is shown that the entropy production ratio approaches (albeit somewhat slower) the $\xi = 1$ value for the finest grid, also indicating convergence for the energy equation.

The entrainment rate for the 2D simulation on the 178 × 160 grid is about 40% higher than that found for the 3D simulation (see Table 1). This can be explained by the higher kinetic energy level in the 2D case, due to which more fluid is entrained from the top layer. This also may indicate that the contribution of the spanwise vortices to entrainment (which is present in the 3D case only) is relatively small.

A well-known, fundamental difference between 2D and 3D flows is the scale direction to which kinetic energy transfers. Whereas in 2D flows kinetic energy cascades to larger scales (called the inverse energy cascade), it cascades to smaller scales in 3D flows. The difference in 2D/3D fluid motion length scales is illustrated by comparing Fig. 11 with Fig. 10. It appears that the motion length scale in the 2D case is much larger than that in the 3D case, though the jet conditions are similar. Further analysis of the momentary velocity fields shows that the 2D field contains three times as much kinetic energy as the 3D field. Fourier analysis reveals that the excess power is present for wavelengths of 0.5–0.2 m, which indicates a large-scale motion (given the 0.445 m width of the box). In addition, the 2D simulated thermocline exhibits more internal waves than its 3D equivalent. The cause for the different kinetic energy level is probably a result of the different direction in which kinetic energy cascades in 2D and 3D flows.

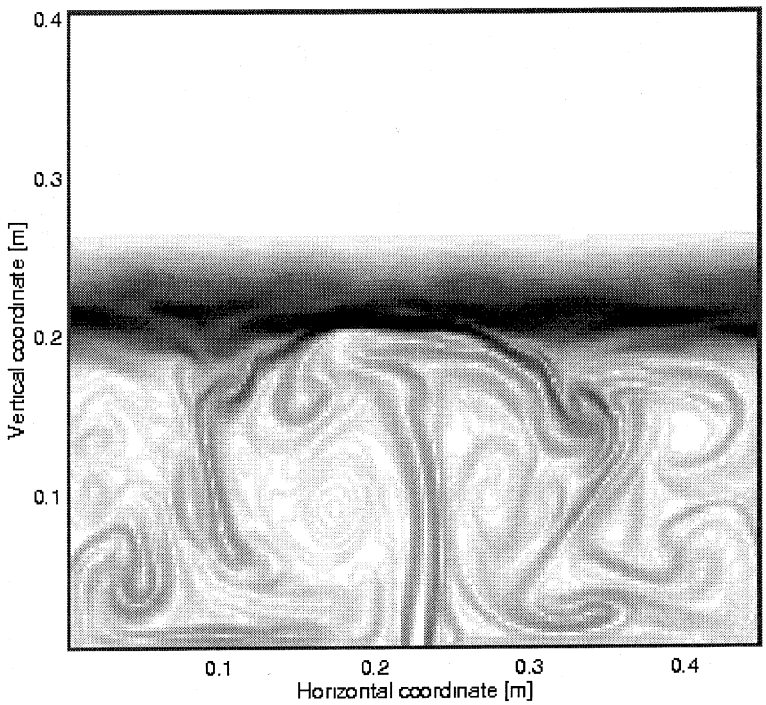

Fig. 11. Calculated entropy production rate for 2D case (white = 10^{-5} W m^{-3} K^{-1}, black = 10^{1} W m^{-3} K^{-1}).

A drawback of the 3D simulation is the intensive memory and CPU usage, which imposes limits with respect to simulation time and spatial resolution. Therefore, in the light of future store optimisation, a relevant question is how well the entrainment process is represented by a (much faster and more refined) 2D-numerical simulation. The argument is that, though 3D information is lost, a 2D representation might provide information which is sufficiently accurate for optimisation purposes. From the present study it may be concluded that the main features of the flow are well presented with a 2D simulation. The spanwise vortices, which are only present in the 3D case, seem to have a minor contribution to the entrainment rate. The difference in the entrainment rate is of the order of 40%, which may lead to the conclusion that 2D calculations might well be used for store optimisation.

7. Closure

The primary goal of the research, gaining insight into the thermocline dynamics in a thermally stratified store, is met by a combined experimental and numerical analysis of the jet destratifying box. With respect to this, the side-by-side experimental and 3D-numerical analyses show to be complementary; where the experiment is a true realisation of the thermocline entrainment process, the numerical simulation provides the temporal and spatial resolution for detailed analysis.

The simplified store model, in which the thermocline propagates due to entrainment alone, facilitates accurate and easy observation of the interface phenomena. In addition, this model is easier and simpler to handle, both numerically and experimentally, than an actual two-layer store. The fluorescent dye and particle tracking experiments gave a clear view on the thermocline dynamics and the entrainment mechanisms involved.

The jet destratifying flow pattern can be described by a buckling jet, which crosses the bottom layer and collides with the thermocline. During collision, inhomogeneous penetration and back flow occurs. At the point where the jet flows back into the bottom layer, the interface between the rebounding jet and the stagnant fluid detaches from the upper layer, and upper-layer fluid is dragged into the bottom layer. After detachment, the dragged-down fluid filament becomes unstable due to overturning motions, resulting in Kelvin–Helmholtz-like waves. Subsequently the fluid filament is completely mixed with bottom-layer fluid by the action of stretching and folding stimulated diffusion.

Due to entrainment, the thermocline is kept sharp. As a result, entropy is mainly produced within the thermocline. In the collision area of the jet with the thermocline the entrainment mechanisms observed are restricted to cusps and wave breaking. At the position where overturning motions take place the shear layer has already detached from the upper layer and entrainment is not expected to play an important role any more. From a comparison with 2D simulations it may be concluded that the spanwise vortices are of minor importance with respect to the total entrainment rate.

For store optimisation, 2D-numerical simulations seem to provide sufficient accuracy. For an identical grid spacing and nearly identical time step, a 2D-numerical simulation predicts an entrainment velocity which is 40% higher than that found in the corresponding 3D-numerical simulation. For 2D simulation more kinetic energy is present at large scales than in a comparable 3D simulation. In addition, the thermocline exhibits a higher level of internal waves. Comparison of 2D- and 3D-simulation results shows that 2D simulation of thermally stratified stores is prone to inverse energy cascade for kinetic energy.

References

[1] O.O. Aderibigre, N. Rajaratnam, Erosion of loose beds by circular impinging vertical turbulent jets, Journal of Hydraulic Research 34 (1996) 19–33.
[2] C. Staquet, J. Sommeria, Internal waves, turbulence and mixing in stratified flows, Journal of Fluid Mechanics 314 (1996) 349–371.
[3] H.J.S. Fernando, Turbulent mixing in stratified fluids, Annual Review of Fluid Mechanics 23 (1991) 455–493.
[4] D.J. Carruthers, J.C.R. Hunt, Velocity fluctuations near an interface between a turbulent region and a stably stratified layer, Journal of Fluid Mechanics 165 (1986) 475–501.
[5] P.F. Linden, Mixing in stratified fluids, Geophysical and Astrophysical Fluid Dynamics 13 (1979) 3–23.
[6] M.W. Wildin, Diffuser design for naturally stratified thermal storage, ASHRAE Transactions AT 90-13-4 (1990) 1094–1102.
[7] J. Meijer, H. Koch, H. Bretschneider, C.W. Schreck, Drucklose Langzeitwärmespeicher Teil II: Be- und Entladevorgänge, Brennstoff Wärme Kraft 35 (1983) 23–26.
[8] Z. Lavan, J. Thompson, Experimental study of thermally stratified hot water storage tanks, Solar Energy 19 (1977) 519–524.
[9] M.A. Hussain, M.W. Wildin, Studies of mixing on the inlet side of the thermocline in diurnal stratified storage, in: Proceedings of the 5th International Conference on Thermal Energy Storage: Thermastock 91, Scheveningen, 1991, pp. 8.5-1–8.5-7.
[10] J. van Berkel, Mixing in thermally stratified energy stores, Solar Energy 58 (1996) 203–211.
[11] J. van Berkel, C.C.M. Rindt, A.A. van Steenhoven, Modelling of two-layer stratified stores, Solar Energy 67 (1999) 65–78.
[12] G.C. Christodoulou, Interfacial mixing in stratified flows, Journal of Hydraulic Research 24 (1986) 77–92.
[13] P.F. Kundu, Fluid Mechanics, Academic Press, London, 1990.

[14] J. van Berkel, Thermocline entrainment in stratified energy stores, Ph.D. thesis, Eindhoven University of Technology, Eindhoven, The Netherlands, 1997.
[15] F.H. Harlow, J.E. Welch, Numerical calculation of time-dependent viscous incompressible flow of fluid with free surface, Physics of Fluids 8 (1965).
[16] F.T.M. Nieuwstadt, Direct and large-eddy simulation of free convection, in: Proceedings of the 9th International Heat Transfer Conference, American Society of Mechanical Engineers, New York, 1990, pp. 37–47.
[17] R.J.M. Bastiaans, C.C.M. Rindt, F.T.M. Nieuwstadt, A.A. van Steenhoven, Direct and large-eddy simulation of the transition of two- and three-dimensional plane plumes in a confined enclosure, International Journal of Heat and Mass Transfer 43 (2000) 2375–2393.
[18] M.J.B.M. Pourquié, Large-eddy simulation of a turbulent jet, Ph.D. thesis, Delft University of Technology, Delft, The Netherlands, 1994.
[19] B.P. Leonard, J.E. Drummond, Why you should not use 'hybrid', 'power law' or related exponential schemes for convective modelling; there are much better alternatives, International Journal for Numerical Methods in Fluids 20 (1995) 421–442.
[20] B. Dalziel, Decay of rotating turbulence; some particle tracking experiments, in: F.T.M. Nieuwstadt (Ed.), Proceedings of the Symposium on Flow Visualisation and Image Analysis, Kluwer Academic Publishers, Dordrecht, 1993.
[21] W.J.A. Dahm, C.M. Scheil, G. Tryggvason, Dynamics of vortex interaction with a density interface, Journal of Fluid Mechanics 205 (1989) 1–43.
[22] A. Bejan, Entropy Generation through Heat and Fluid Flow, Wiley, New York, 1982.
[23] I. Danaila, J. Dusek, F. Anselmet, Space structure of the free, unsteady, round, homogeneous jet at low Reynolds numbers, in: S. Gavrilakis (Ed.), Proceedings of the Sixth European Turbulence Conference, Kluwer Academic Publishers, Dordrecht, 1996, pp. 11–14.
[24] A.J. Cotel, R.E. Breidenthal, Vortex persistance, in: S. Gavrilakis (Ed.), Proceedings of the Sixth European Turbulence Conference, Kluwer Academic Publishers, Dordrecht, 1996, pp. 95–98.
[25] J.E. Simpson, Gravity Currents in the Environment and the Laboratory, Ellis Horwood/Wiley, Chichester, 1987.
[26] D. Liepmann, M. Gharib, The role of streamwise vorticity in the near field entrainment of round jets, Journal of Fluid Mechanics 245 (1992) 643–668.
[27] N. Baba, Streamwise vortices near a density interface, Dynamics of Atmospheres and Oceans 24 (1996) 95–105.